Science Advances
AAAS

advances.sciencemag.org/cgi/content/full/6/41/eabc3699/DC1

Supplementary Materials for

Asteroid (101955) Bennu's weak boulders and thermally anomalous equator

B. Rozitis*, A. J. Ryan, J. P. Emery, P. R. Christensen, V. E. Hamilton, A. A. Simon, D. C. Reuter, M. Al Asad, R.-L. Ballouz, J. L. Bandfield, O. S. Barnouin, C. A. Bennett, M. Bernacki, K. N. Burke, S. Cambioni, B. E. Clark, M. G. Daly, M. Delbo, D. N. DellaGiustina, C. M. Elder, R. D. Hanna, C. W. Haberle, E. S. Howell, D. R. Golish, E. R. Jawin, H. H. Kaplan, L. F. Lim, J. L. Molaro, D. Pino Munoz, M. C. Nolan, B. Rizk, M. A. Siegler, H. C. M. Susorney, K. J. Walsh, D. S. Lauretta

*Corresponding author. Email: benjamin.rozitis@open.ac.uk

Published 8 October 2020, *Sci. Adv.* **6**, eabc3699 (2020)
DOI: 10.1126/sciadv.abc3699

The PDF file includes:

Other Supplementary Material for this manuscript includes the following:

(available at advances.sciencemag.org/cgi/content/full/6/41/eabc3699/DC1)

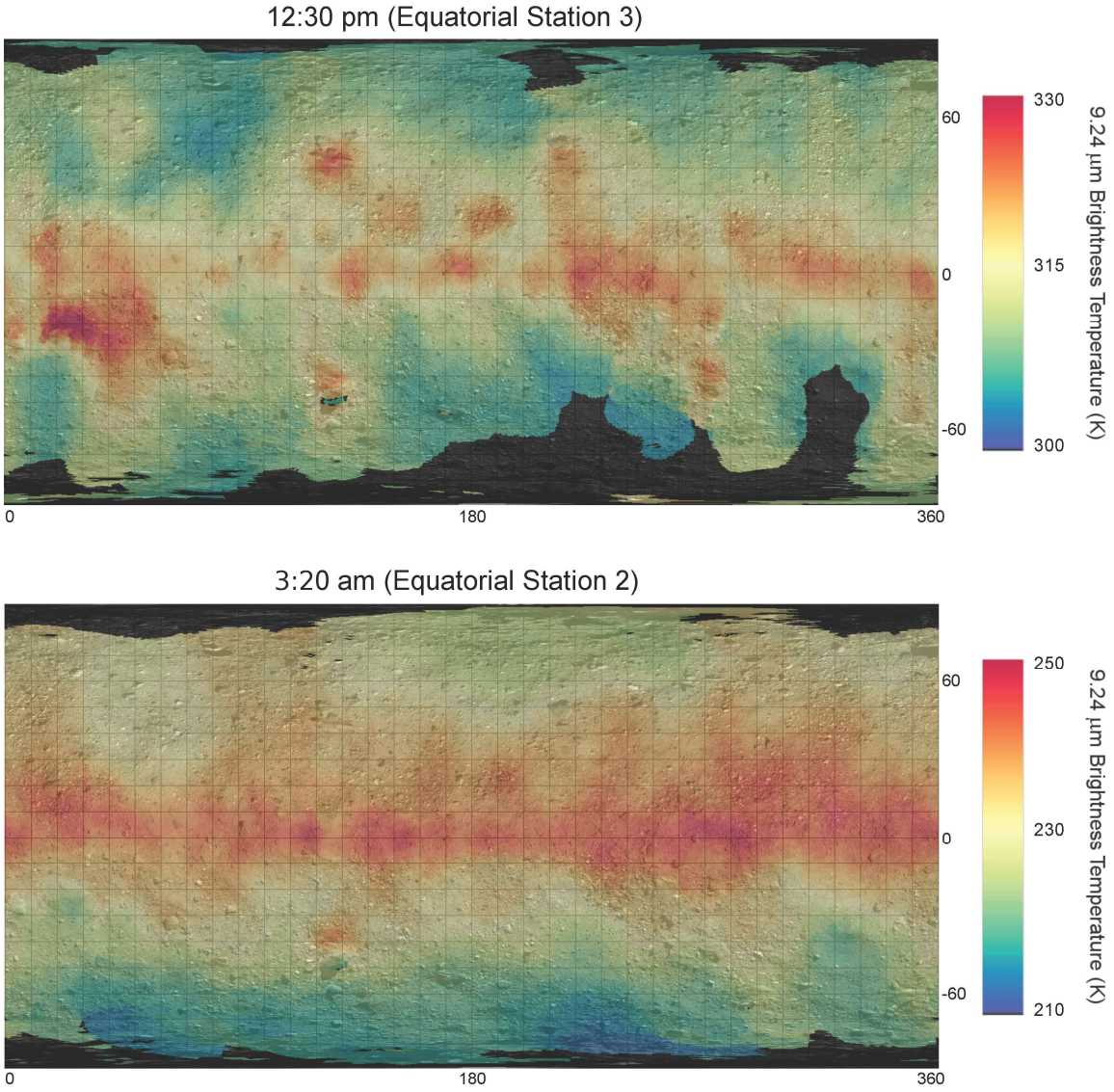

Fig. S1. Maps of 9.24 μm brightness temperature on (101955) Bennu for the 12:30 pm daytime (top) and 3:20 am nighttime (bottom) Equatorial Stations. The dark regions are where spots were omitted because the surface temperature is close to the OTES detector temperature (see Materials and Methods) or where there was limited coverage near the poles.

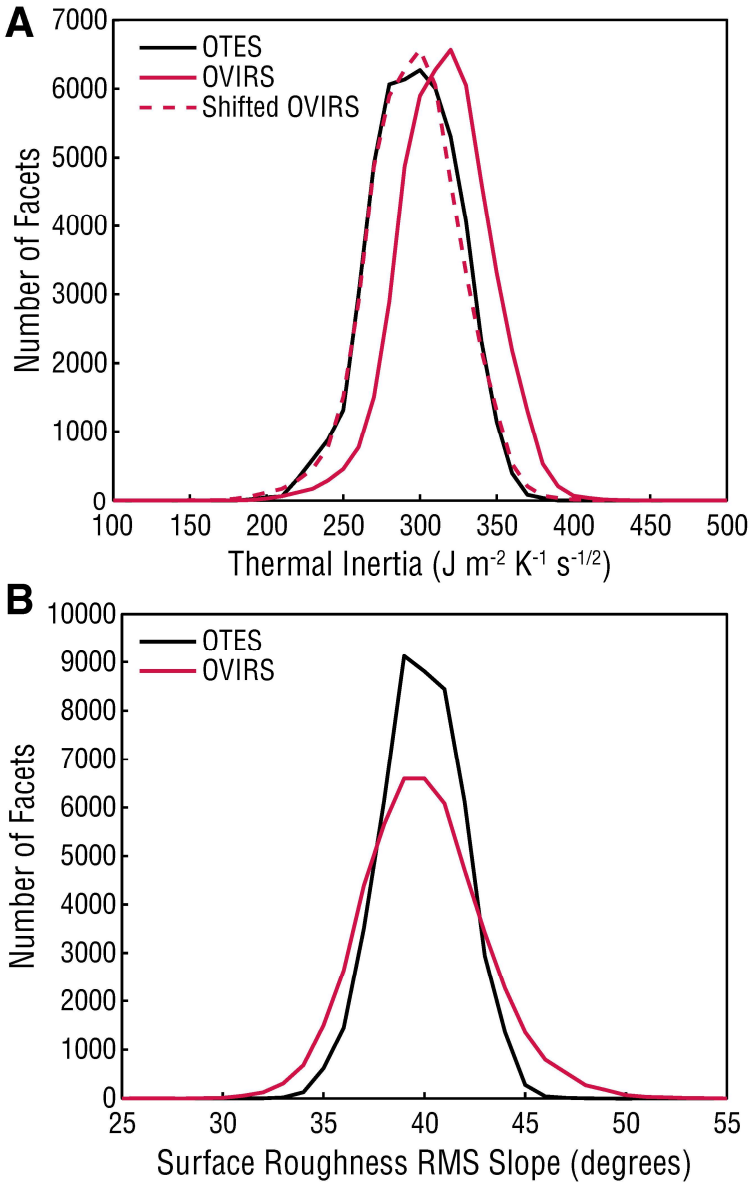

Fig. S2. Frequency distributions of thermal inertia (A) and surface roughness (B) derived for (101955) Bennu from OTES and OVIRS data. The OVIRS thermal inertia distribution is in good agreement with the OTES distribution when its thermal inertia values are systematically shifted by –20 J m^{-2} K^{-1} $s^{-1/2}$.

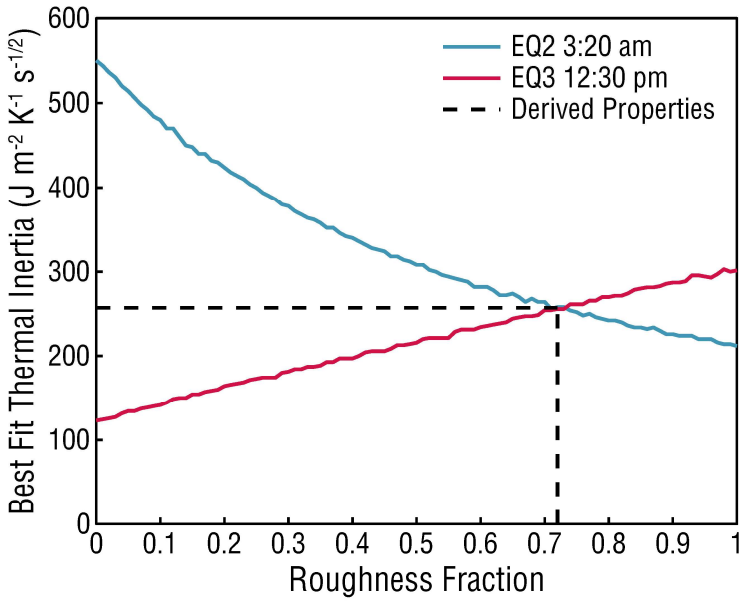

Fig. S3. Examples of opposing daytime and nighttime degeneracies between thermal inertia and surface roughness resulting from model fits to OTES data acquired at two different local times of day. These examples are from the first 6-m facet specified in the SPC/OLA v34 shape model of (101955) Bennu. The degeneracies are resolved where the two curves intersect.

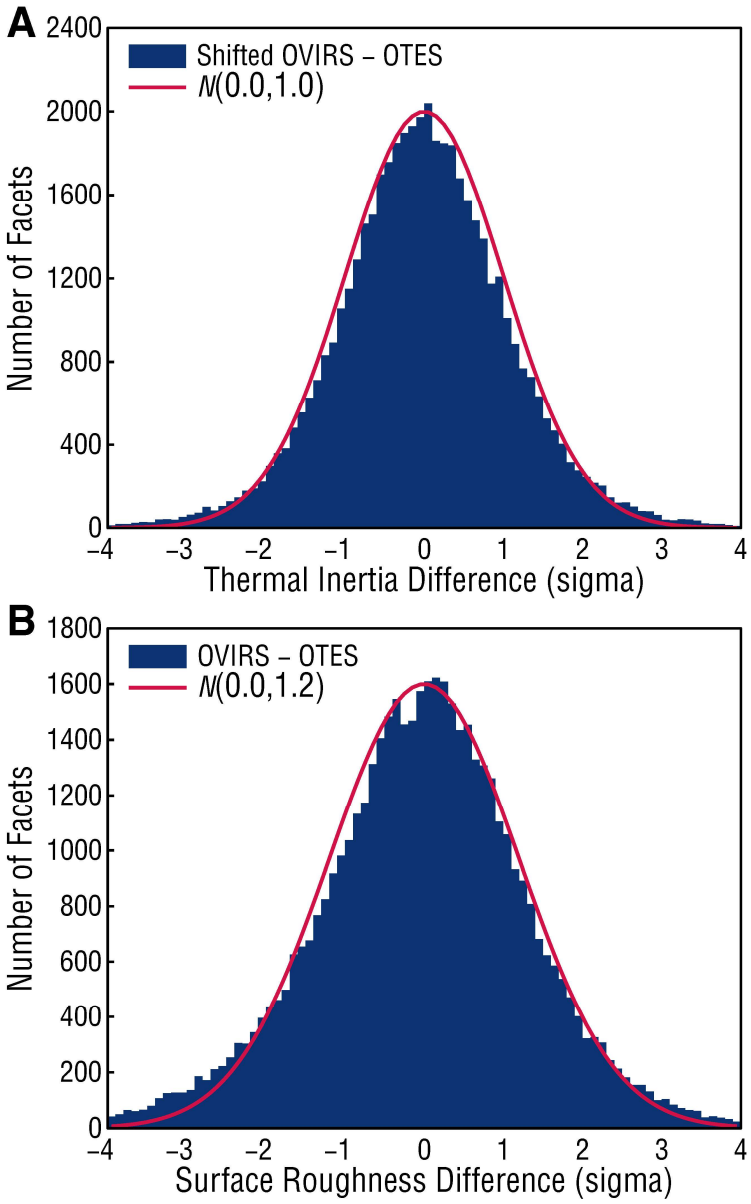

Fig. S4. Frequency distributions of uncertainty-normalized dispersions of thermal inertia (A) and surface roughness (B) between thermal models of (101955) Bennu based on OTES and OVIRS data. The best-fit Gaussian functions are shown for comparison.

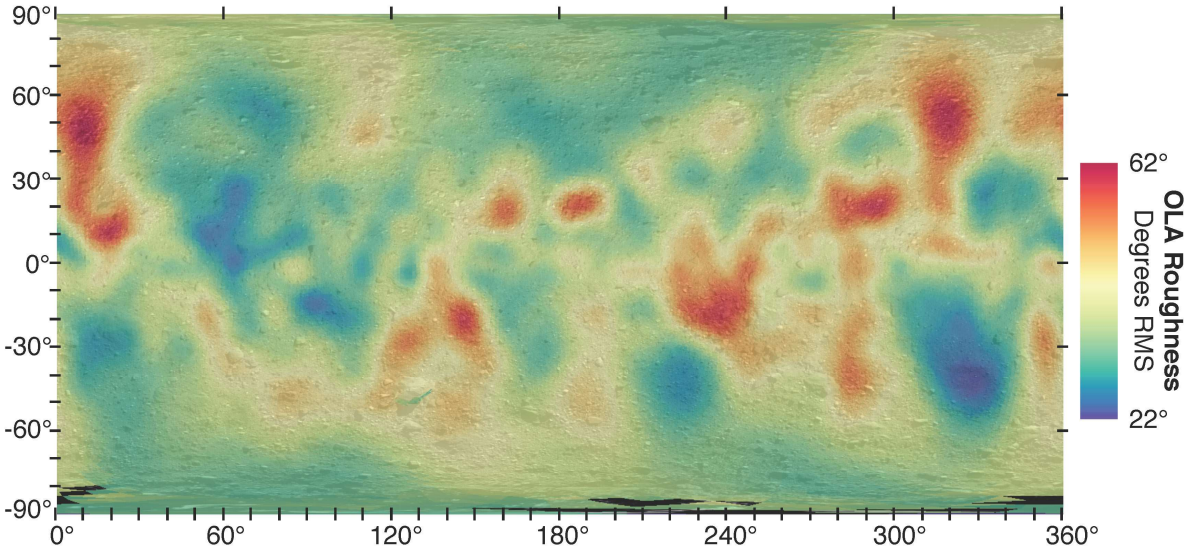

Fig. S5. Surface roughness of (101955) Bennu as determined from the OLA v16 20-cm shape model. The spatial-resolution of this map has been degraded to match that of OTES shown in Fig. 1.

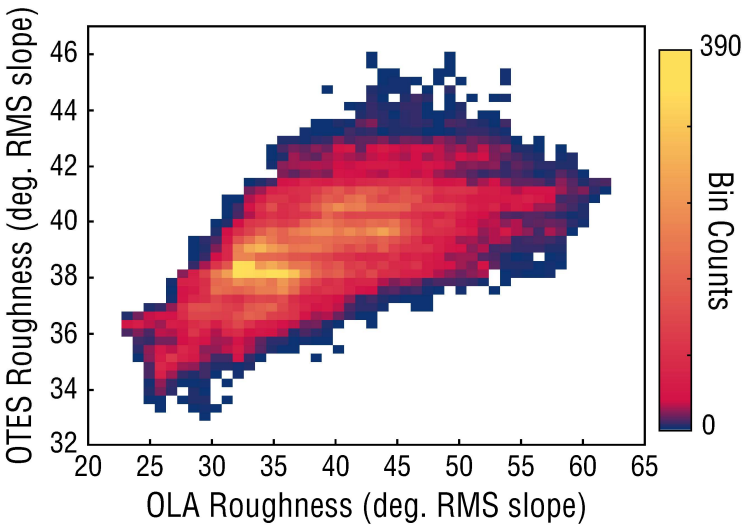

Fig. S6. 2D histogram of OTES roughness and OLA roughness on (101955) Bennu.

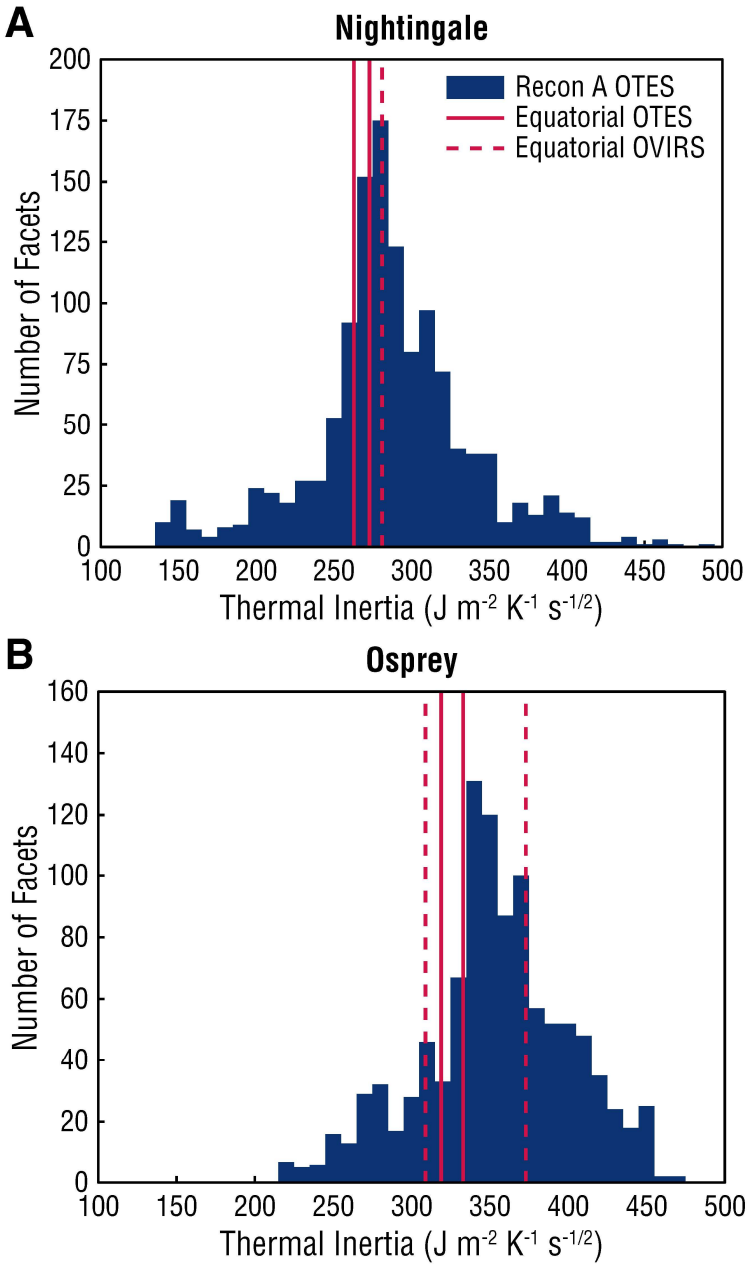

Fig. S7. Thermal inertia distributions for the Nightingale (A) and Osprey (B) candidate sample sites derived from OTES data collected during Recon A. From Fig. 4, the thermal inertia values within 20-m radii of the candidate sample site coordinates were binned to allow comparison with the low-spatial-resolution values determined from the global analysis. In particular, the vertical lines correspond to the 1σ uncertainty ranges of the global analysis results.

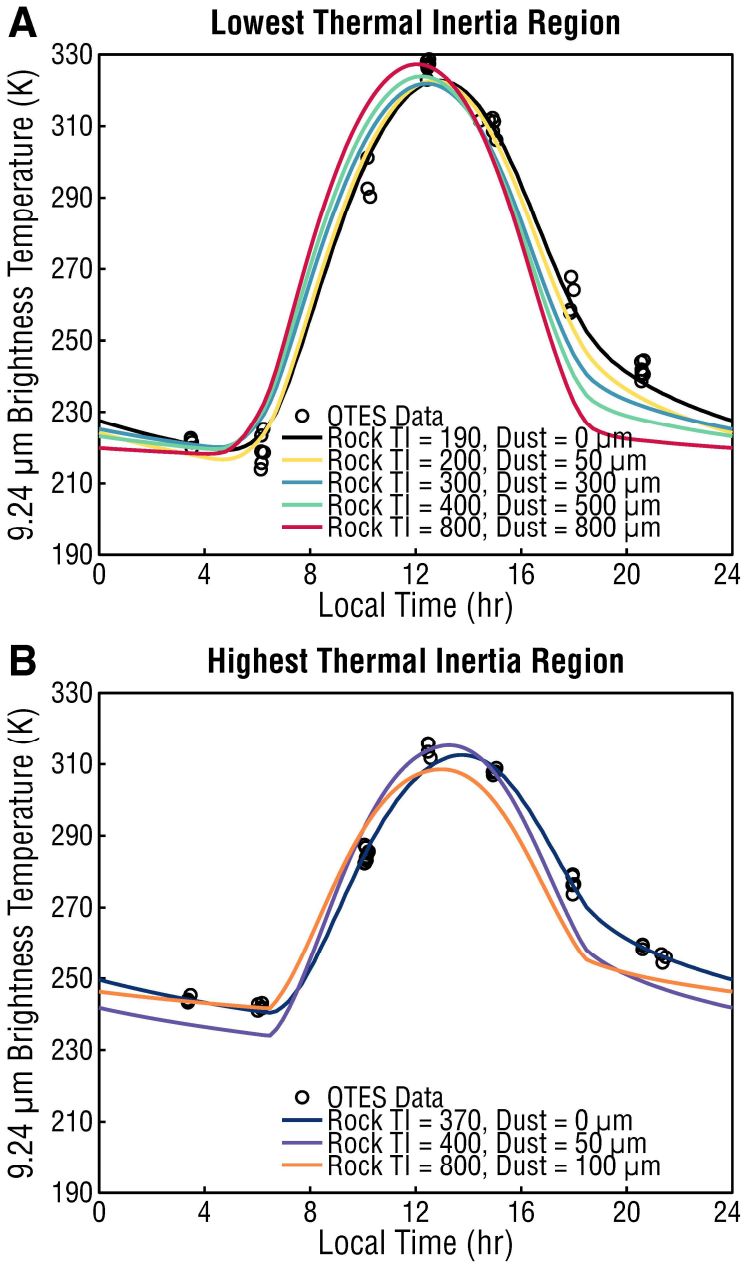

Fig. S8. The influence of thin layers of dust on the modeled diurnal temperature curves for the regions of lowest (A) and highest (B) thermal inertia identified on (101955) Bennu. As in Fig. 2, the OTES 9.24-µm brightness temperatures have been scaled to a common heliocentric distance, and also adjusted to a common spot geometry. The OTES temperature data can only be fit with an absent or a very thin layer of dust (<50 µm thick) along with a low thermal inertia value for the underlying rock.

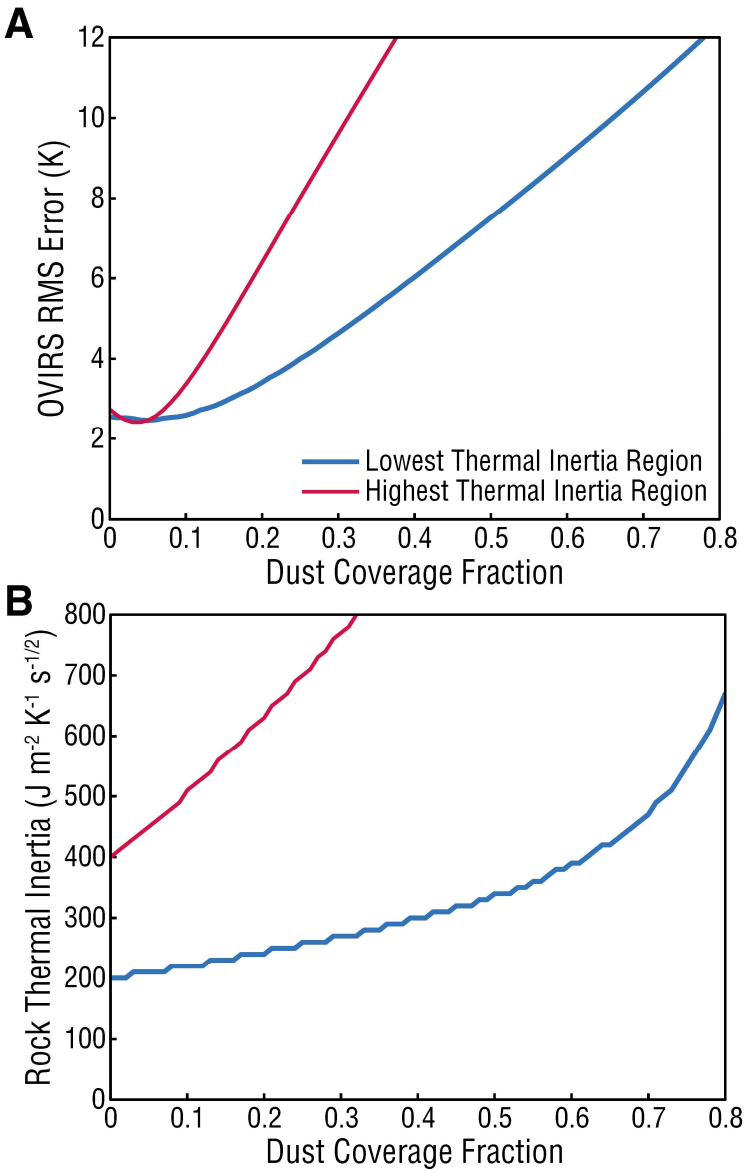

Fig. S9. Results of fitting a lateral dust mixing model to OVIRS data of the regions with lowest and highest thermal inertia on (101955) Bennu. The OVIRS RMS error (A) and best-fit rock thermal inertia (B) were calculated as a function of dust coverage fraction assuming a lunar-like thermal inertia of 50 J m^{-2} K^{-1} $s^{-1/2}$ for the dust component.

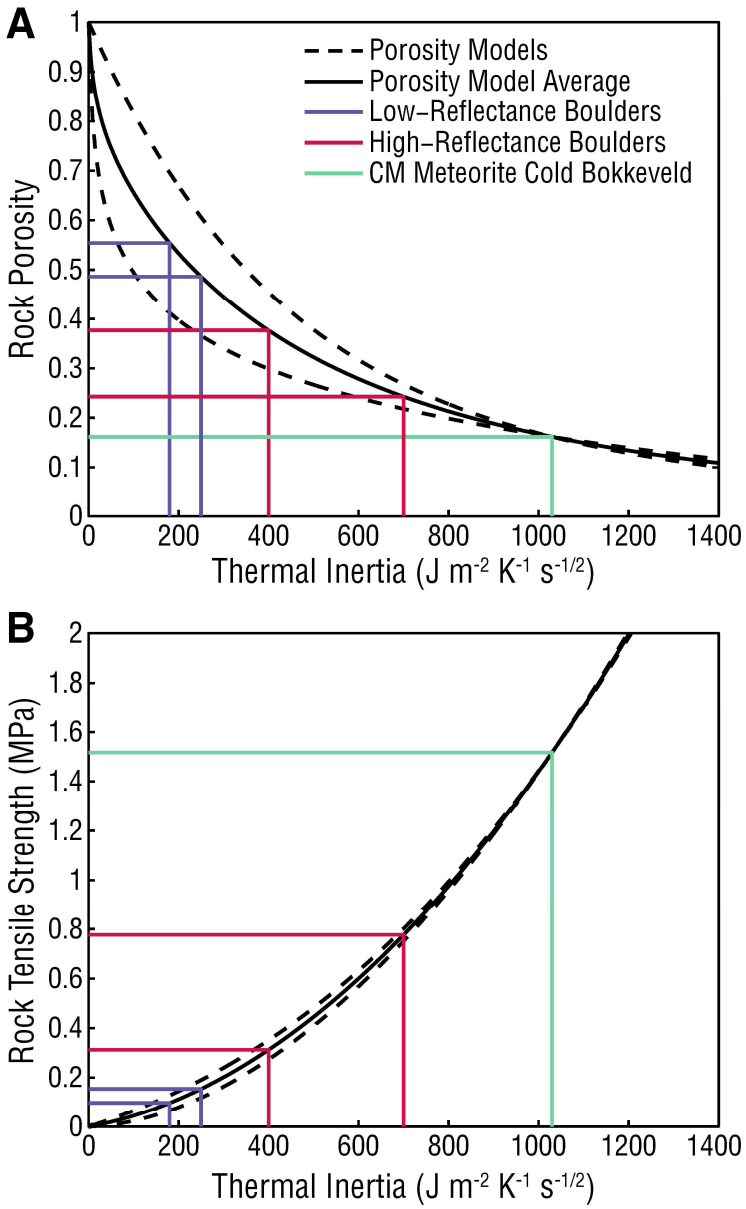

Fig. S10: Rock porosity (A) and tensile strength (B) calculations for the low- and high-reflectance boulders on (101955) Bennu. Calculations were performed using the models of (*31*, *50*, *51*).

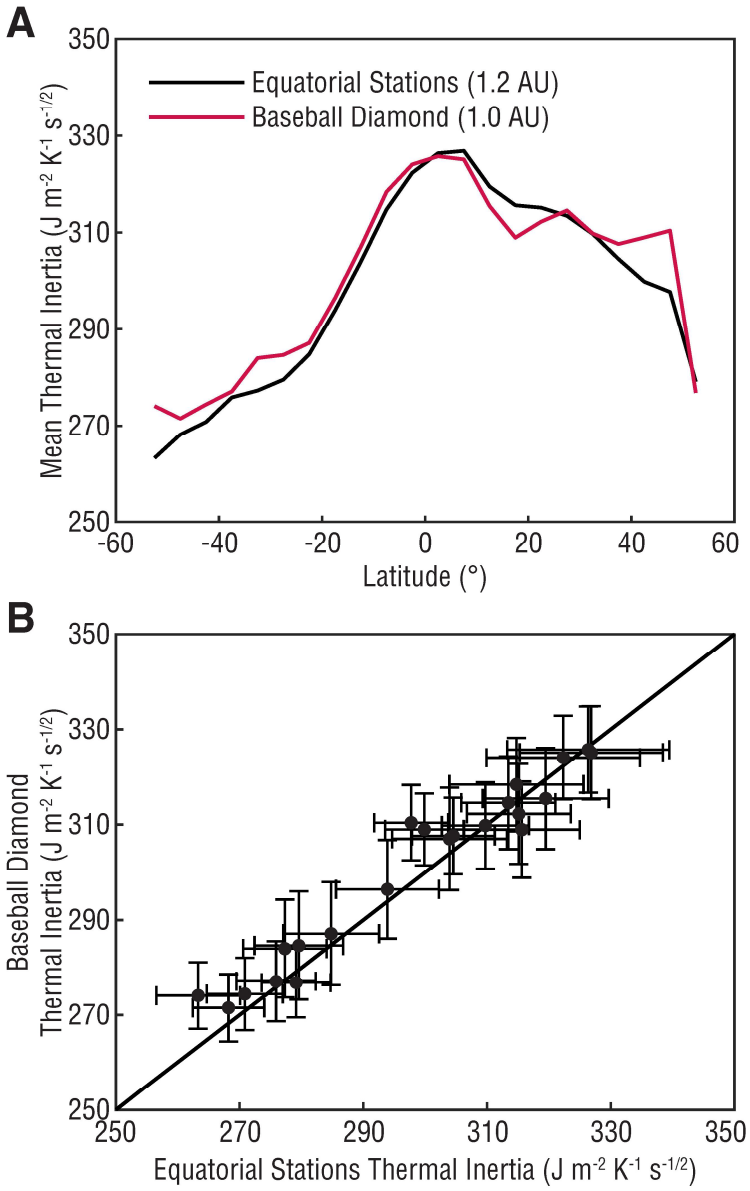

Fig. S11. Comparison of thermal inertia derived from Baseball Diamond Flyby 1 data against thermal inertia derived from Equatorial Stations data for (101955) Bennu. As in Fig. 5, the global map values have been averaged within latitude bins of 5° in width (A). The change in thermal inertia between these two mission phases (B), or more precisely with the heliocentric distance of Bennu, is far less than the mean thermal inertia uncertainty of ~10 J m^{-2} K^{-1} $s^{-1/2}$ (error bars), indicating that Bennu's thermal inertia is not strongly temperature-dependent.

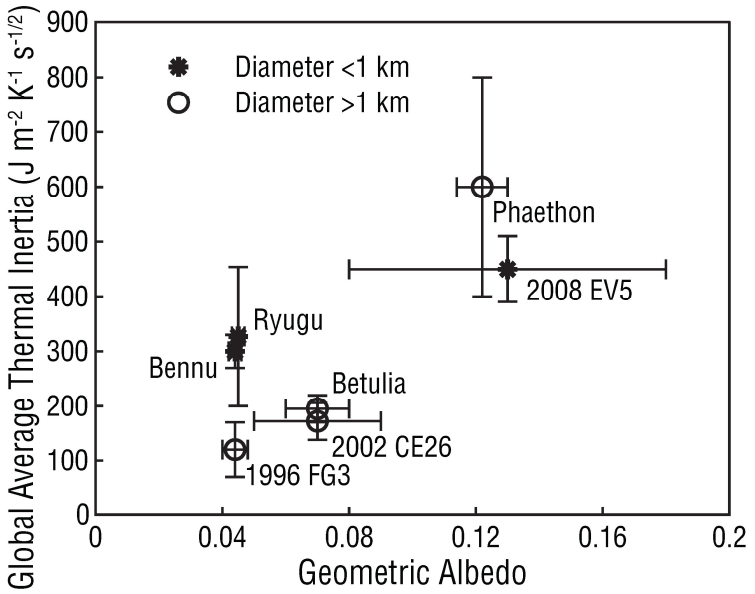

Fig. S12. Global average thermal inertia versus geometric albedo for C-complex NEAs. Included NEAs are those that have well-constrained shapes and pole orientations. References: Bennu (this work), Betulia (*87*), Phaethon (*85*), Ryugu (*29*, *30*), 1996 FG3 (*86*), 2002 CE26 (*87*), and 2008 EV5 (*88*).

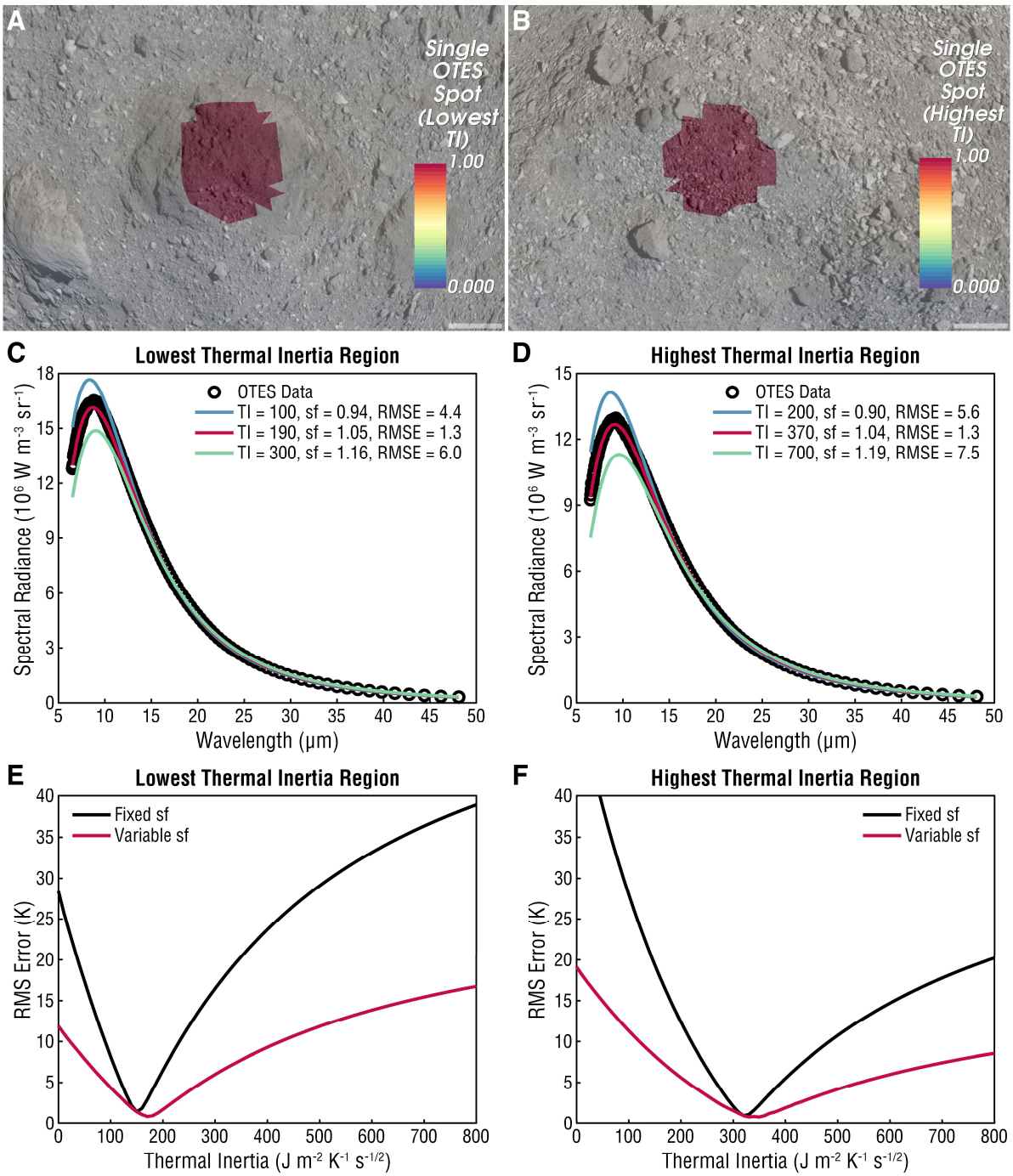

Fig. S13. Examples of fitting a single OTES spot. Projections of a single OTES spot onto the regions of lowest (A) and highest (B) thermal inertia on (101955) Bennu. Model fits to OTES radiance spectra for the regions of lowest (C) and highest (D) thermal inertia. RMS error as a function of thermal inertia for the regions of lowest (E) and highest (F) thermal inertia. In the model fitting, fixed surface roughness RMS slopes of 36° and 40° were applied to the regions of lowest and highest thermal inertia, respectively.

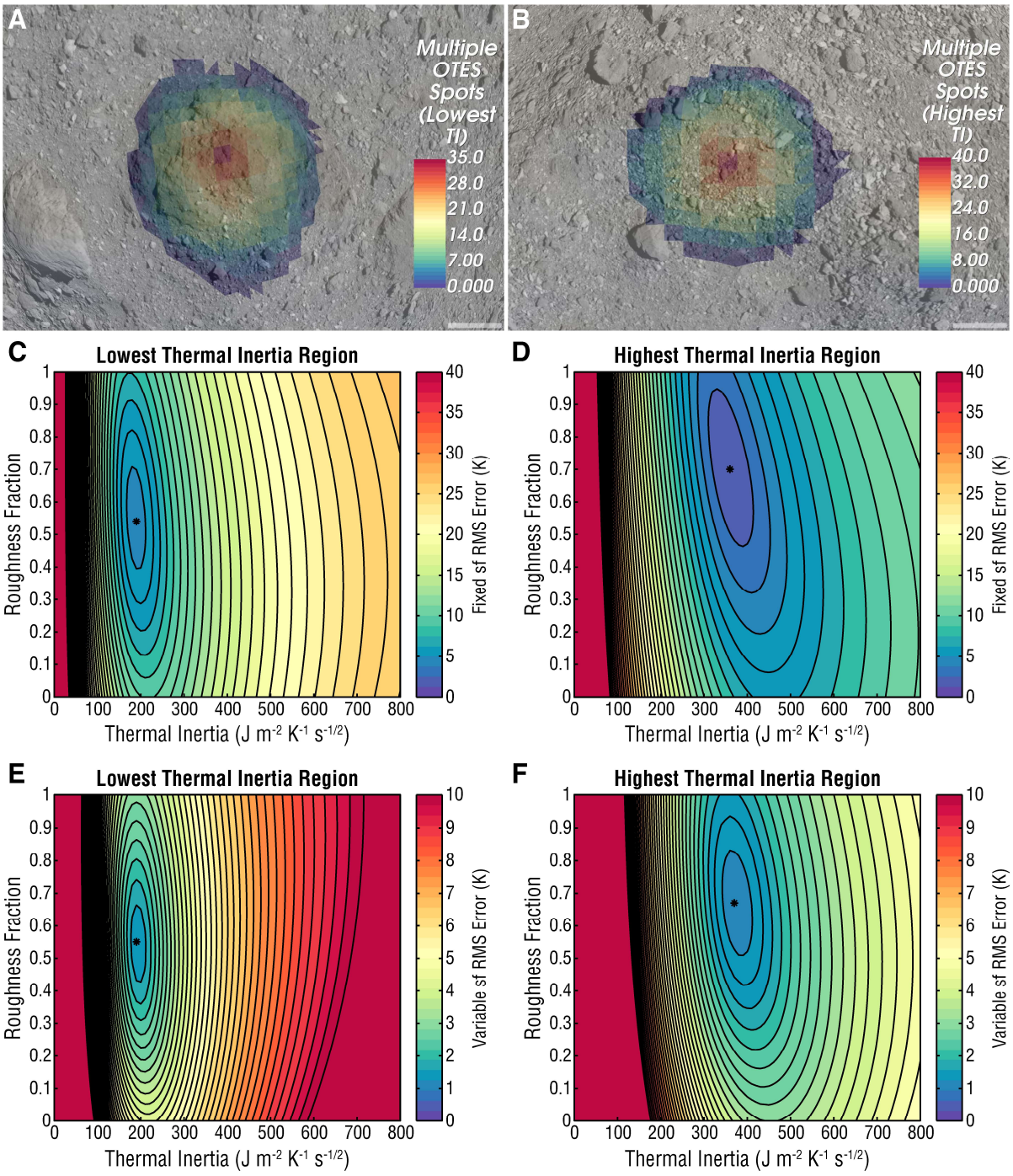

Fig. S14. Examples of fitting multiple OTES spots. Projections of multiple OTES spots onto the regions of lowest (A) and highest (B) thermal inertia on (101955) Bennu. RMS error as a function of thermal inertia and roughness fraction for the regions of lowest (C) and highest (D) thermal inertia for fixed scale factors. RMS error as a function of thermal inertia and roughness fraction for the regions of lowest (E) and highest (F) thermal inertia for variable scale factors.

The RMS error contours are spaced by 1 and 0.25 K for fixed (C and D) and variable (E and F) scale factors, respectively.

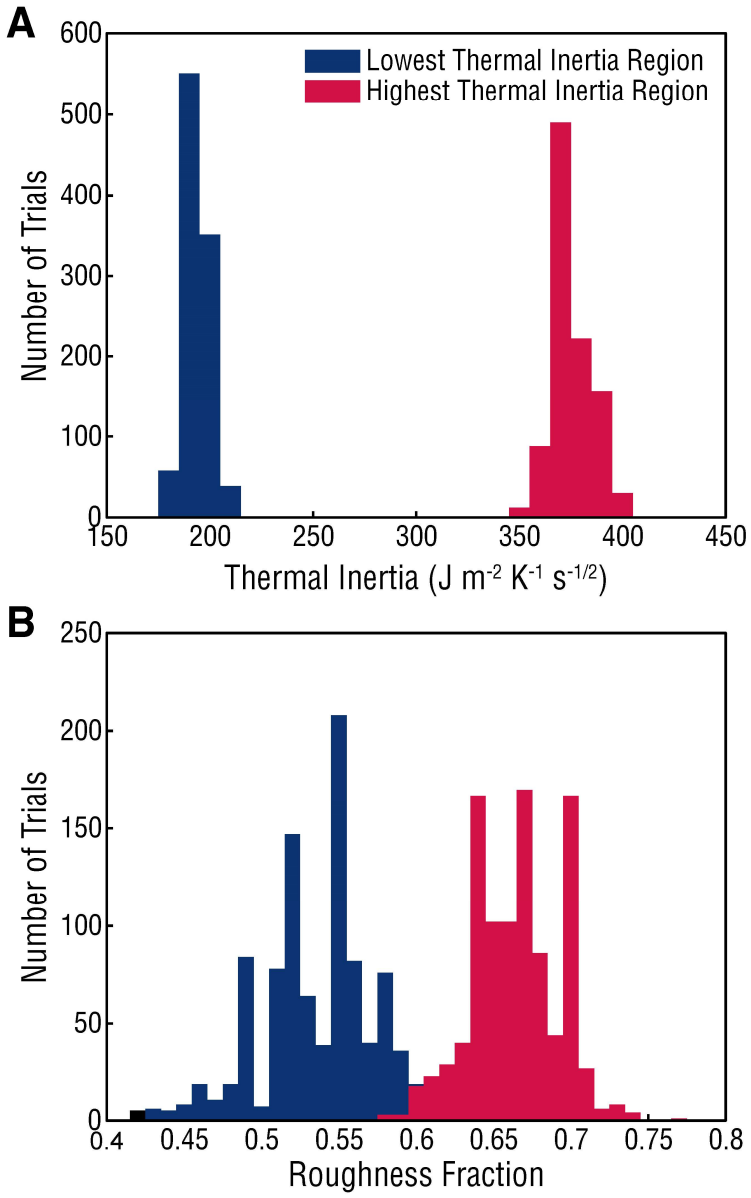

Fig. S15. Histograms of thermal inertia (A) and roughness fraction (B) resulting from Monte Carlo uncertainty analyses of OTES data collected during the Equatorial Stations for the regions with lowest and highest thermal inertia on (101955) Bennu.

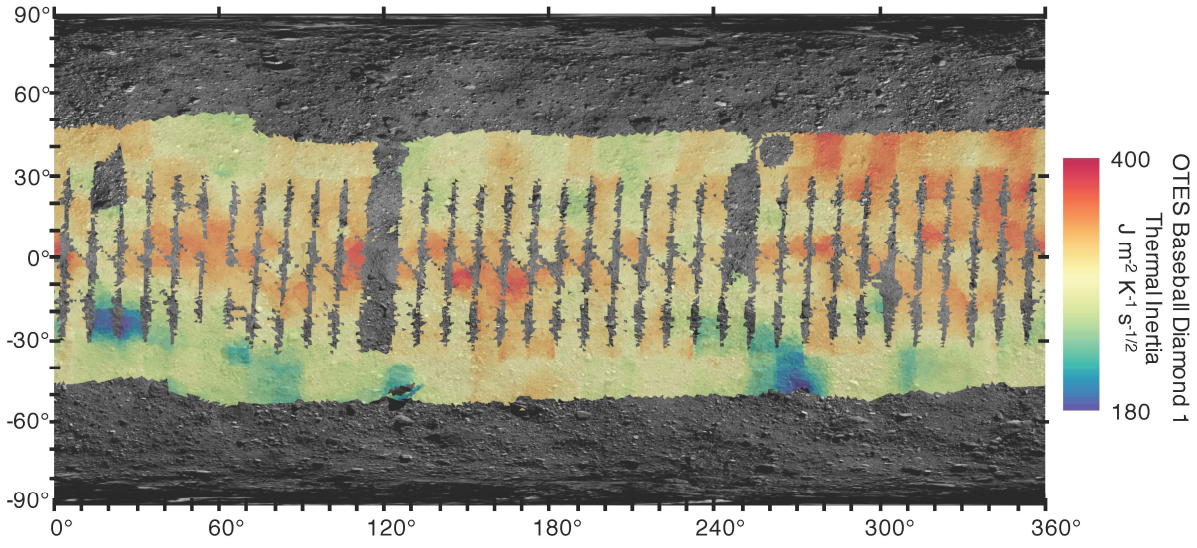

Fig. S16. Baseball Diamond Flyby 1 thermal inertia map of (101955) Bennu.

Table S1. Positional geometry of (101955) Bennu and the number of infrared observations used for thermophysical modelling. EQ, Equatorial Station.

Mission Phase	Observation Local Solar Time (hr)	Date and Time (UTC)	Heliocentric Distance (AU)	Heliocentric Ecliptic Longitude (°)	Heliocentric Ecliptic Latitude (°)	Number of OTES Spots	Number of OVIRS Spots
BBD 1	12:30	03/07/19 19:30	0.997312	134.7198	4.4420	2550	Not used
EQ1	15:00	04/25/19 20:00	1.158725	178.0373	0.4203	2201	7538
EQ2	03:20	05/02/19 20:00	1.180560	183.2469	–0.1300	2798	4953
EQ3	12:30	05/09/19 20:00	1.201503	188.2712	–0.6598	2789	7193
EQ4	10:00	05/16/19 20:00	1.221425	193.1283	–1.1671	2543	6168
EQ5	06:00	05/23/19 20:00	1.240216	197.8354	–1.6505	3057	5351
EQ6	20:40	05/30/19 20:00	1.257785	202.4085	–2.1094	2899	2770
EQ7	18:00	06/06/19 20:00	1.274053	206.8627	–2.5432	3281	3238
Recon A - Osprey	08:20-15:10	10/12/19 22:00	1.302811	280.9751	–5.9608	2046	Not used
Recon A - Nightingale	08:50-16:10	10/26/19 21:00	1.274604	289.6182	–5.7532	2109	Not used

Table S2. Summary of results for the different global analyses of (101955) Bennu performed using OTES data.

Shape Model	Bolometric Emissivity	Scale Factor	RMS Error (K)	Thermal Inertia ($J\ m^{-2}\ K^{-1}\ s^{-1/2}$)	Thermal Inertia Uncertainty ($J\ m^{-2}\ K^{-1}\ s^{-1/2}$)	Surface Roughness (°)	Surface Roughness Uncertainty (°)
SPC v20	0.95	1 (fixed)	2.9 ± 0.7	291 ± 28	9 ± 4	39.8 ± 3.0	0.9 ± 0.4
SPC v20	0.95	0.99 ± 0.03	1.3 ± 0.2	298 ± 28	9 ± 3	40.1 ± 2.6	0.9 ± 0.4
SPC/OLA v34	0.90	1 (fixed)	3.1 ± 0.5	283 ± 27	9 ± 3	40.2 ± 2.5	0.9 ± 0.4
SPC/OLA v34	0.90	1.04 ± 0.04	1.3 ± 0.2	302 ± 38	9 ± 4	33.6 ± 3.3	1.0 ± 0.6
SPC/OLA v34	0.95	1 (fixed)	2.7 ± 0.6	290 ± 28	9 ± 3	39.6 ± 2.4	0.9 ± 0.4
SPC/OLA v34	0.95	0.99 ± 0.03	1.2 ± 0.2	296 ± 28	8 ± 3	39.9 ± 2.0	0.8 ± 0.4
SPC/OLA v34	1.00	1 (fixed)	3.3 ± 0.5	297 ± 29	9 ± 4	39.1 ± 2.3	0.8 ± 0.4
SPC/OLA v34	1.00	0.94 ± 0.03	1.2 ± 0.2	293 ± 23	8 ± 3	45.4 ± 2.4	0.7 ± 0.3
OLA v16	0.95	1 (fixed)	2.6 ± 0.6	288 ± 29	9 ± 3	39.1 ± 2.1	0.9 ± 0.4
OLA v16	0.95	0.99 ± 0.03	1.2 ± 0.2	295 ± 29	8 ± 3	39.1 ± 1.7	0.8 ± 0.4

Table S3. Summary of results for the different global analyses of (101955) Bennu performed using OVIRS data.

Shape Model	Bolometric Emissivity	Scale Factor	RMS Error (K)	Thermal Inertia ($J\ m^{-2}\ K^{-1}\ s^{-1/2}$)	Thermal Inertia Uncertainty ($J\ m^{-2}\ K^{-1}\ s^{-1/2}$)	Surface Roughness (°)	Surface Roughness Uncertainty (°)
SPC v20	0.95	1 (fixed)	3.2 ± 1.1	318 ± 29	13 ± 6	40.2 ± 3.9	1.5 ± 0.8
SPC/OLA v34	0.95	1 (fixed)	3.0 ± 0.9	316 ± 29	12 ± 6	40.0 ± 3.0	1.4 ± 0.8
OLA v16	0.95	1 (fixed)	2.9 ± 0.8	313 ± 30	11 ± 5	39.0 ± 2.5	1.4 ± 0.8

Table S4. Summary of dust and rock thermophysical properties used in the dust layering analysis.

Material	Thermal Conductivity ($W\ m^{-1}\ K^{-1}$)	Density ($kg\ m^{-3}$)	Specific Heat Capacity ($J\ kg^{-1}\ K^{-1}$)	Thermal Inertia ($J\ m^{-2}\ K^{-1}\ s^{-1/2}$)
Dust	2.800×10^{-3}	1190	750	50
Rock with low thermal inertia	4.246×10^{-2}	1257	750	200
Rock with low thermal inertia	7.424×10^{-2}	1617	750	300
Rock with medium thermal inertia	1.147×10^{-1}	1860	750	400
Rock with high thermal inertia	3.659×10^{-1}	2333	750	800

Movie S1. Animation of daytime brightness temperature variations on (101955) Bennu when viewed at a phase angle of 0°. These brightness temperatures were computed at a wavelength of 9.24 μm using the OTES-derived thermal inertia and surface roughness maps shown in Fig. 1, and are plotted on the same scale as movie S3 to allow a direct comparison to the nighttime brightness temperature variations. A morning-afternoon temperature asymmetry is apparent due to the time delaying effect of thermal inertia. Additionally, Bennu's large low-reflectance boulders standout as the hottest features because of their comparatively low thermal inertia.

Movie S2. Same as movie S1 but plotted on a narrower temperature scale to emphasize the daytime brightness temperature variations.

Movie S3. Animation of nighttime brightness temperature variations on (101955) Bennu when viewed at a phase angle of 180°. Bennu cools during the night due to the lack of direct sunlight heating its surface but this rate of cooling is reduced for areas of high thermal inertia. As such, the high thermal inertia equator stands out as being the hottest feature during Bennu's night. These brightness temperatures are plotted on the same scale as movie S1 to allow a direct comparison to the daytime brightness temperature variations.

Movie S4. Same as movie S3 but plotted on a narrower temperature scale to emphasize the nighttime brightness temperature variations.